Pair-truncated shell-model analysis for doubly-odd nuclei around mass 130

Koji Higashiyama[1,*] and Naotaka Yoshinaga[2,†]
[1]*Department of Physics, Chiba Institute of Technology, Narashino, Chiba 275-0023, Japan*
[2]*Department of Physics, Saitama University, Saitama City 338-8570, Japan*
(Received 22 May 2013; revised manuscript received 5 August 2013; published 17 September 2013)

Low-lying states for doubly-odd nuclei in the mass $A \sim 130$ region are investigated using a pair-truncated shell model. Energy levels of the low-lying states for doubly-odd nuclei, ^{132}Cs, ^{130}Cs, ^{134}La, and ^{132}La, are reproduced very well along with the electromagnetic transitions. The analysis of the wave functions reveals band structure for doublet bands built on the $\nu h_{11/2} \otimes \pi h_{11/2}$ configuration, showing various angular-momentum configurations of the unpaired neutron and the unpaired proton, weakly coupled with the quadrupole collective excitations of the even-even part of the nucleus.

DOI: 10.1103/PhysRevC.88.034315 PACS number(s): 21.60.Cs, 21.60.Ev, 27.60.+j

I. INTRODUCTION

The study of the nearly degenerate doublet bands in doubly-odd nuclei is a subject of special interest in recent years. A vast amount of the experimental information about such pairs of bands built on the $\nu h_{11/2} \otimes \pi h_{11/2}$ configuration has been accumulated in the mass $A \sim 130$ region [1–9]. The excitation mechanism of the doublet bands was explained by the nuclear chirality in angular-momentum coupling, which was predicted by Frauendorf and Meng [10]. In that picture, three angular momenta of the even-even part of the nucleus, the unpaired neutron, and the unpaired proton are perpendicular to each other in the intrinsic frame. They can form either a left-handed or right-handed geometrical configuration, which cannot be transformed into one another by rotation. These configurations are energetically equivalent, and two degenerate bands are constructed as linear combinations of these. The chiral structure of the doublet bands was investigated theoretically in the framework of the tilted axis cranking model [1,2,6,11], the particle-rotor model [3,12], and the core-quasiparticle coupling model [5,7,13]. However, the results of many recent experiments and analyses do not necessarily support this interpretation [14–17].

The pair-truncated shell model (PTSM) provides a reasonable theoretical framework for a full shell model to describe the nuclear collective motions and the single-particle degrees of freedom on equal footing [18–29]. In the simplest version of the PTSM, the full shell-model space is restricted within the SD subspace where angular momenta zero (S) and two (D) collective pairs are used as the building blocks. In describing odd-mass and/or doubly-odd nuclei, additional unpaired nucleons are added to the even-even nuclear states. Based on this framework, systematic studies were carried out for the even-even and the odd-mass nuclei in the mass $A \sim 130$ region, and excellent agreement with the experimental data was achieved for both energy levels and electromagnetic properties [24]. The same set of interactions was applied to doubly-odd nuclei, and excellent agreement with the experimental data was achieved for the energy levels of the doublet bands and the electromagnetic transitions, especially for the staggering of the ratios $B(M1; I \to I-1)/B(E2; I \to I-2)$ for the yrast states [26–28]. Through the analysis of the PTSM wave functions, it has been confirmed that the doublet bands turn out to be constructed by a weak coupling of various angular-momentum configurations of an unpaired neutron and an unpaired proton, i.e., the *chopsticks configurations* [26,27], with the quadrupole collective excitations of the even-even part of the nucleus.

For a description of the doublet bands in doubly-odd nuclei, we have recently proposed a simple but essential model, i.e., a quadrupole coupling model (QCM) [30–33], where the classical core representing the even-even part of the nucleus couples with a neutron and a proton in the high-j intruder orbitals through a quadrupole-quadrupole interaction. The structure of the doublet bands in the mass $A \sim 130$ region was extensively studied in terms of the QCM, and good agreement with the experimental data was achieved for both the energy spectra and features of electromagnetic transitions [30,31]. By analyzing the QCM wave functions, the excitation mechanism predicted on the basis of the previous PTSM calculations [26–28] has been reconfirmed.

The purpose of the present paper is to reinvestigate the excitation mechanism of the doubly-odd nuclei, $^{132}_{55}$Cs, ^{130}Cs, $^{134}_{57}$La, and ^{132}La, in terms of the PTSM. The model space and the effective Hamiltonian are defined as in our earlier systematic calculations for the even-even, odd-mass, and doubly-odd nuclei around the mass $A \sim 130$ [29]; a doubly-closed $^{132}_{50}$Sn core is used and the valence space consists of five $0g_{7/2}$, $1d_{5/2}$, $1d_{3/2}$, $0h_{11/2}$, and $2s_{1/2}$ orbitals in the major shell of $50 \leqslant N(Z) \leqslant 82$ for neutrons (protons). The effective interactions consist of single-particle energies and monopole and quadrupole pairing plus quadrupole-quadrupole interactions, whose strengths are assumed to be linearly changed as functions of the number of nucleons so as to describe the level schemes of the even-even and odd-mass nuclei. In order to clarify the internal structure of the yrast and yrare states built on the $\nu h_{11/2} \otimes \pi h_{11/2}$ configuration, a powerful method is employed, where we construct the wave functions with *specific configurations* in the shell-model space and then calculate the overlaps between them and the yrast and

*koji.higashiyama@it-chiba.ac.jp
†yoshinaga@phy.saitama-u.ac.jp

yrare states. Detailed information on the internal structure of these states can be obtained in this method.

The paper is organized as follows: In Sec. II, we give a brief outline of the PTSM and its effective interactions in the model space. In Sec. III, the PTSM calculations are carried out for even-even nuclei, $^{132}_{54}$Xe, ^{130}Xe, $^{134}_{56}$Ba, and ^{132}Ba. In Sec. IV, the same set of interactions is applied to the doubly-odd nuclei, ^{132}Cs, ^{130}Cs, ^{134}La, and ^{132}La. Theoretical energy spectra and electromagnetic properties are compared with the experimental data. In Sec. V, we clarify the structure of the doublet bands through the analysis of their wave functions. In Sec. VI, we conclude the paper with a summary. In the Appendix, we give a brief description of the specific wave function that is used for the analysis of the doublet bands.

II. THEORETICAL FRAMEWORK

The nuclear shell model is one of the most successful general models to describe various aspects of nuclear structure. It is desirable to use the full 50–82 configuration space for studying the doublet bands in the mass $A \sim 130$ region, but the shell-model calculation in this space is impractical at present due to its huge dimension. To avoid this problem, we adopt the PTSM [18–29], where the full shell-model space is restricted within the subspace of collective pairs. In its simplest version of the PTSM, i.e., the SD version of the PTSM, even-even nuclear states are constructed by the S and D collective pairs. The S and D pair-creation operators are defined as

$$S^\dagger = \sum_j \alpha_j A_0^{\dagger(0)}(jj), \tag{1}$$

$$D_M^\dagger = \sum_{j_1 j_2} \beta_{j_1 j_2} A_M^{\dagger(2)}(j_1 j_2), \tag{2}$$

where the structure coefficients α and β are determined by a variation in each nucleus as in Refs. [19,24,29]. The nucleon pair-creation operator with angular momentum J, and its projection M, is defined as

$$\begin{aligned} A_M^{\dagger(J)}(j_1 j_2) &= \sum_{m_1 m_2} (j_1 m_1 j_2 m_2 | JM) c_{j_1 m_1}^\dagger c_{j_2 m_2}^\dagger \\ &= \left[c_{j_1}^\dagger c_{j_2}^\dagger \right]_M^{(J)}, \end{aligned} \tag{3}$$

where $(j_1 m_1 j_2 m_2 | JM)$ stands for a Clebsch-Gordan coefficient, $c_{jm}^\dagger$ represents either a neutron-hole creation operator or a proton-particle creation operator, and (j, m) represents a set of quantum numbers necessary to specify the state (n, ℓ, j, m). In this mass region we treat neutrons as holes and protons as particles so that $N = 82$ and $Z = 50$ become the nearest closed shells. The S and D pairs are constructed in each neutron or proton space separately.

A many-body SD-pair state of like nucleons is constructed by applying the S and D pair-creation operators on the inert core $|-\rangle$ as

$$|S^{n_s} D^{n_d}(I\eta)\rangle = (S^\dagger)^{n_s} (D^\dagger)^{n_d} |-\rangle, \tag{4}$$

where I is an angular momentum of the SD-pair state, and η is an additional quantum number required to completely specify the state. The numbers of the S and D pairs are denoted as n_s and n_d, respectively. The angular-momentum coupling is carried out exactly, but we abbreviate its notation.

In order to describe odd-mass and doubly-odd nuclei, we need to expand the model space to include an unpaired nucleon in addition to the SD-pair state [24,29]. If the nucleon creation operator $c_{jm}^\dagger$ is applied to the SD-pair state, the odd-nucleon state, i.e., the SD-pairs plus one-particle state, is constructed as

$$|j S^{n_s} D^{n_d}(I\eta)\rangle = c_j^\dagger |S^{n_s} D^{n_d}(I'\eta)\rangle, \tag{5}$$

where I' is the angular momentum of the SD-pair state, I is the angular momentum of the SD-pair plus one-particle state, and η is an additional quantum number. Due to this extension, the PTSM can treat even-even, odd-mass, and doubly-odd nuclei on the same footing. Using the SD-pair plus one-particle state in both neutron and proton spaces, we can express the many-body wave function of the doubly-odd nucleus as

$$|\Phi(I\eta)\rangle = [|j_\nu S^{\bar{n}_s} D^{\bar{n}_d}(I_\nu \eta_\nu)\rangle \otimes |j_\pi S^{n_s} D^{n_d}(I_\pi \eta_\pi)\rangle]^{(I)}, \tag{6}$$

where $2(\bar{n}_s + \bar{n}_d) + 1$ and $2(n_s + n_d) + 1$ are the numbers of valence neutron holes $\bar{N}_\nu$ and proton particles N_π, respectively. The SD-pair states and the SD-pair plus one-particle states are generally nonorthogonal and the Schmidt orthogonalization procedure is adopted.

As an effective interaction, we employ the monopole and quadrupole pairing plus quadrupole-quadrupole interaction. The effective shell-model Hamiltonian is written as

$$\hat{H} = \hat{H}_\nu + \hat{H}_\pi + \hat{H}_{\nu\pi}, \tag{7}$$

where $\hat{H}_\nu$, $\hat{H}_\pi$, and $\hat{H}_{\nu\pi}$ represent the neutron interaction, the proton interaction, and the neutron-proton interaction, respectively. The interaction among like nucleons $\hat{H}_\tau$ ($\tau = \nu$ or π) consists of spherical single-particle energies, monopole-pairing (MP) interaction, quadrupole-pairing (QP) interaction, and quadrupole-quadrupole (QQ) interaction,

$$\begin{aligned} \hat{H}_\tau = &\sum_{jm} \varepsilon_{j\tau} c_{jm\tau}^\dagger c_{jm\tau} - G_{0\tau} \hat{P}_\tau^{\dagger(0)} \hat{P}_\tau^{(0)} \\ &- G_{2\tau} \hat{P}_\tau^{\dagger(2)} \tilde{\hat{P}}_\tau^{(2)} - \kappa_\tau : \hat{Q}_\tau \cdot \hat{Q}_\tau :, \end{aligned} \tag{8}$$

where :: represents normal ordering, and $c_{jm\tau}$ is either a neutron-hole annihilation operator or a proton-particle annihilation operator. The monopole pair-creation operator $\hat{P}_\tau^{\dagger(0)}$, the quadrupole pair-creation operator $\hat{P}_{M\tau}^{\dagger(2)}$, and the quadrupole operator $\hat{Q}_{M\tau}$ are defined by

$$\hat{P}_\tau^{\dagger(0)} = \sum_j \frac{\sqrt{2j+1}}{2} A_{0\tau}^{\dagger(0)}(jj), \tag{9}$$

$$\hat{P}_{M\tau}^{\dagger(2)} = \sum_{j_1 j_2} Q_{j_1 j_2} A_{M\tau}^{\dagger(2)}(j_1 j_2), \tag{10}$$

$$\tilde{\hat{P}}_{M\tau}^{(2)} = (-)^M \hat{P}_{-M\tau}^{(2)}, \tag{11}$$

$$\hat{Q}_{M\tau} = \sum_{j_1 j_2} Q_{j_1 j_2} \left[c_{j_1\tau}^\dagger \tilde{c}_{j_2\tau} \right]_M^{(2)}, \tag{12}$$

with

$$\tilde{c}_{jm\tau} = (-1)^{j-m} c_{j-m\tau}, \tag{13}$$

$$Q_{j_1 j_2} = -\frac{\langle j_1 \| r^2 Y^{(2)} \| j_2 \rangle}{\sqrt{5}}, \tag{14}$$

where $A^{\dagger(J)}_{M\tau}(j_1 j_2)$ stands for the nucleon-pair creation operator given by Eq. (3).

The interaction between neutrons and protons $\hat{H}_{\nu\pi}$ is taken as

$$\hat{H}_{\nu\pi} = -\kappa_{\nu\pi}\, \hat{Q}_\nu \cdot \hat{Q}_\pi, \tag{15}$$

where $\hat{Q}_\tau$ is the quadrupole operator defined by Eq. (12). In the present scheme, harmonic oscillator basis states with the oscillator parameter $b = \sqrt{\hbar/(M\omega)}$ are used as the single-particle basis states. The detailed framework of the model is reported in Refs. [24,29].

The shell-model Hamiltonian in Eq. (7) is diagonalized in terms of the many-body basis wave functions in Eq. (6) as

$$\hat{H}\, |I^\pi \eta\rangle = E(I^\pi \eta)\, |I^\pi \eta\rangle\,, \tag{16}$$

where $|I^\pi \eta\rangle$ is the normalized eigenvector for the ηth state with total spin I and parity π, and $E(I^\pi \eta)$ is the eigenenergy for the state $|I^\pi \eta\rangle$.

III. NUMERICAL RESULTS FOR EVEN-EVEN NUCLEI

For the nuclei in the mass $A \sim 130$ region, several valence neutron holes and valence proton particles are coupled to the doubly-closed shells $N = 82$ and $Z = 50$. Since the valence neutron holes (proton-particles) occupy the $0g_{7/2}$, $1d_{5/2}$, $1d_{3/2}$, $0h_{11/2}$, and $2s_{1/2}$ orbitals, we take into account the full $50 \sim 82$ configuration space for neutrons (protons), where valence neutrons (protons) are treated as holes (particles). For the single-particle energies and the interaction strengths, we have used exactly the same values given by the set of equations used in previous systematic studies of $A \sim 130$ nuclei [29]. The single-particle energies $\varepsilon_{j\tau}$ ($\tau = \nu$ or π) employed in the present calculations are listed in Table I.

The determined functional dependencies of the correction terms σ_ν and σ_π to the constant single-particle energies are as follows (in MeV):

$$\sigma_\nu = +0.02\bar{N}_\nu + 0.06 N_\pi - 0.02, \tag{17}$$

$$\sigma_\pi = -0.02\bar{N}_\nu - 0.15 N_\pi + 0.15, \tag{18}$$

where $\bar{N}_\nu$ indicates the number of valence neutron-holes and N_π indicates the number of valence proton particles. Note that the experimental excitation energies of ^{131}Sn are given when $\bar{N}_\nu = 1$ and $N_\pi = 0$, and those of ^{133}Sb are given when $\bar{N}_\nu = 0$ and $N_\pi = 1$.

TABLE I. Adopted single-particle energies $\varepsilon_{j\tau}$ ($\tau = \nu$ or π) for neutron holes or proton particles (in MeV). The numerals are extracted from experimental excitation energies in Refs. [34–36], and the correction terms σ_ν and σ_π are given in Eq. (18).

j	$2s_{1/2}$	$0h_{11/2}$	$1d_{3/2}$	$1d_{5/2}$	$0g_{7/2}$
$\varepsilon_{j\nu}$	0.332	$0.242 + \sigma_\nu$	0.000	1.655	2.434
$\varepsilon_{j\pi}$	$2.990 + \sigma_\pi$	$2.793 + \sigma_\pi$	$2.708 + \sigma_\pi$	0.962	0.000

For these valence spaces, the two-body interaction strengths were determined by a least-squares fit of the low-lying energy levels as for the even-even Xe, Ba, and Ce isotopes [29]. To reproduce overall spectra of the preceding nuclei, the linear dependence of the interaction strengths on the number of the valence neutron holes and/or proton particles was introduced. The adopted interaction strengths are as follows (G_0 of MP interaction in units of MeV, and G_2 of QP interaction and κ of QQ interaction both in units of MeV/b^4):

$$\begin{aligned}
G_{0\nu} &= 0.150 - 0.010\bar{N}_\nu - 0.002 N_\pi,\\
G_{2\nu} &= 0.004 + 0.001\bar{N}_\nu + 0.002 N_\pi,\\
\kappa_\nu &= 0.070 - 0.001\bar{N}_\nu + 0.001 N_\pi,\\
G_{0\pi} &= 0.150 - 0.010\bar{N}_\nu,\\
G_{2\pi} &= 0.008 - 0.0005\bar{N}_\nu + 0.001 N_\pi,\\
\kappa_\pi &= 0.020 + 0.002 N_\pi,\\
\kappa_{\nu\pi} &= -0.060 - 0.001\bar{N}_\nu + 0.002 N_\pi.
\end{aligned} \tag{19}$$

The concrete difference between the present and previous PTSM calculations are as follows: In the previous PTSM studies [26–28], the single-particle energies were extracted from experimental excitation energies and were fixed constant for all the nuclei. The previous results for even-even Xe, Ba, Ce, and Nd isotopes reproduced well the energy levels for both the yrast and quasi-γ bands and the intraband and interband $B(E2)$ values [24]. However, the previous results of the odd-mass isotopes were not satisfactory enough to describe the relative positions of the energy levels of positive-parity states and those of negative-parity states, especially for proton-odd nuclei. A similar situation was also seen in the previous PTSM results for the doubly-odd nuclei [27]. The doublet bands with the $\nu h_{11/2} \otimes \pi h_{11/2}$ configuration in theory were reproduced higher in energy than experimental ones. These results clearly indicate a need to shift the single-particle energy of the $0h_{11/2}$ orbital relative to the others. Thus, in the present study, we assume that the single-particle energies of some orbitals besides the $0h_{11/2}$ orbital change linearly with the number of valence particles.

In Fig. 1, the energy spectra of the PTSM are compared with the experimental data for even-even nuclei, ^{132}Xe, ^{130}Xe, ^{134}Ba, and ^{132}Ba. For all the nuclei, the calculations reproduce well the energy levels for both the yrast band and quasi-γ bands (the 2^+_2, 3^+_1, 4^+_2, 5^+_1, and 6^+_2 states). The theoretical $E2$ transition rates and branching ratios also agree well with the experimental data. Some other details were presented in Ref. [29].

IV. NUMERICAL RESULTS FOR DOUBLY-ODD NUCLEI

A. Energy spectra of yrast and yrare states with $\nu h_{11/2} \otimes \pi h_{11/2}$ configuration

Using the set of the interaction strengths mentioned in the previous section, the energy spectra are obtained for

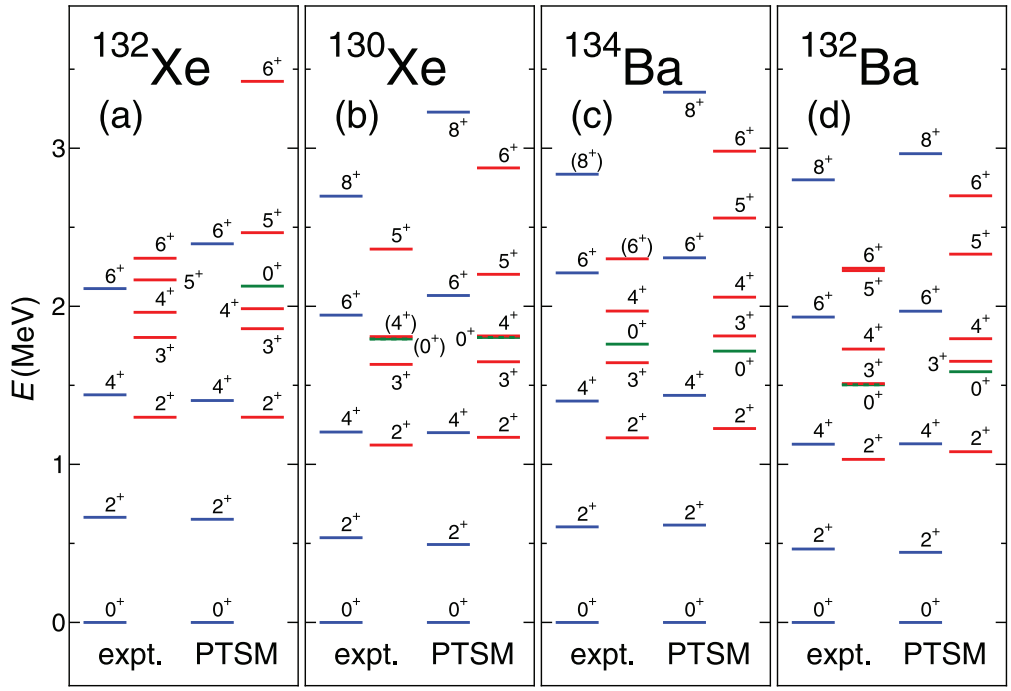

FIG. 1. (Color online) Comparison between experimental energy spectra (expt.) and those of the PTSM (PTSM) for (a) ^{132}Xe, (b) ^{130}Xe, (c) ^{134}Ba, and (d) ^{132}Ba. The level sequences on the left represent the yrast states, and the level sequences on the right represent the 2_2^+, 3_1^+, 4_2^+, 5_1^+, 6_2^+, and 0_2^+ states. The experimental data are taken from Refs. [37–43].

doubly-odd nuclei. In Fig. 2 the experimental energy spectrum based on the $\nu h_{11/2} \otimes \pi h_{11/2}$ configuration is compared with the PTSM calculation for ^{132}Cs (even-even core: ^{132}Xe). In experiment the 6_1^+, 7_1^+, and 8_1^+ states are not observed, but the PTSM calculation predicts the 6_1^+, 7_1^+, and 8_1^+ states to lie near the 9_1^+ state. For the yrast states with spins greater than 9, calculated energy levels are in excellent agreement with the experimental data. For the yrare states, the PTSM calculation reproduces the observed levels at the correct positions, except that some states are not found in experiment.

In Fig. 3, the energy levels of the low-lying states in theory are compared with the experimental data for ^{130}Cs (even-even core: ^{130}Xe). For the yrast states, calculated energy levels are in good agreement with experiment. There is no experimental evidence for the 6_1^+, 7_1^+, and 8_1^+ states, but in theory the 6_1^+, 7_1^+, and 8_1^+ states appear slightly higher in energy than the 9_1^+ state. For the yrare states, the PTSM calculation reproduces the experimental energy levels, although the model predicts a few low-spin states that are not experimentally observed.

In Figs. 4 and 5, the theoretical energy levels of the PTSM are compared with the experimental data for ^{134}La (even-even core: ^{134}Ba) and ^{132}La (even-even core: ^{132}Ba), respectively. Similar to ^{130}Cs, the 7_1^+ and 8_1^+ states are not found in experiment for ^{134}La. In the PTSM calculation, they are located near the 9_1^+ state. For higher spin states, the PTSM gives a reasonable description for the energy levels of the yrast and yrare states. In ^{132}La, the experimental 7_1^+ and 8_1^+ states lie lower in energy than the 9_1^+ state. In theory the 7_1^+ and 8_1^+ states are a bit higher in energy than the 9_1^+ state, but there exists a one-to-one correspondence between the theoretical and experimental levels. For an accurate description of the ordering and position of these low-lying states, we may need higher-angular-momentum pairs such as angular-momentum-four (G) collective pairs and/or hexadecapole interactions, both of which are missing in the present scheme.

B. Electromagnetic transitions

To clarify the band structure with the $\nu h_{11/2} \otimes \pi h_{11/2}$ configuration, we calculate the $M1$ and $E2$ transition rates in the following. The $M1$ transition rate is calculated as

$$B\left(M1; I_\eta^\pi \to J_\xi^\pi\right) = \frac{1}{2I+1} |\langle J^\pi \xi \| \hat{T}(M1) \| I^\pi \eta \rangle|^2, \quad (20)$$

where $|I^\pi \eta\rangle$ represents the wave function for the ηth state with total spin I and parity π given by Eq. (16). The $M1$ transition operator is defined as

$$\hat{T}(M1) = \mu_N \sqrt{\frac{3}{4\pi}} \sum_{\tau=\nu,\pi} [g_{\ell\tau} \hat{\boldsymbol{j}}_\tau + (g_{s\tau} - g_{\ell\tau}) \hat{\boldsymbol{s}}_\tau], \quad (21)$$

where μ_N [$=e\hbar/(2mc)$] represents the nuclear magneton, and $g_{\ell\tau}$ and $g_{s\tau}$ ($\tau = \nu$ or π) represent the gyromagnetic ratios for orbital angular momentum and spin, respectively. The angular momentum and spin operators are denoted as $\hat{\boldsymbol{j}}$ and $\hat{\boldsymbol{s}}$, respectively. The $E2$ transition rate is calculated as

$$B\left(E2; I_\eta^\pi \to J_\xi^\pi\right) = \frac{1}{2I+1} |\langle J^\pi \xi \| \hat{T}(E2) \| I^\pi \eta \rangle|^2. \quad (22)$$

The $E2$ transition operator is defined as

$$\hat{T}(E2) = e_\nu \hat{Q}_\nu + e_\pi \hat{Q}_\pi, \quad (23)$$

where e_τ ($\tau = \nu$ or π) represents the effective charge of the nucleon, and $\hat{Q}_\tau$ is the quadrupole operator with the oscillator

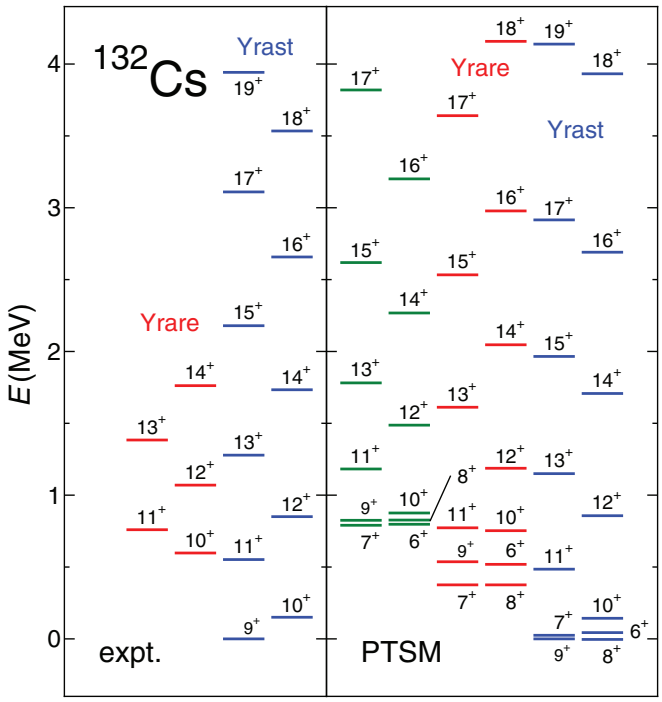

FIG. 2. (Color online) Comparison of experimental energy levels (expt.) based on the $\nu h_{11/2} \otimes \pi h_{11/2}$ configuration with PTSM results (PTSM) for ^{132}Cs. In the right panel, two level sequences of $\Delta I = 1$ on the right represent the yrast band, and two level sequences of $\Delta I = 1$ in the middle, the yrare band. Two levels on the left denote the third lowest-energy states for each total spin I. The experimental data are taken from Refs. [44–46].

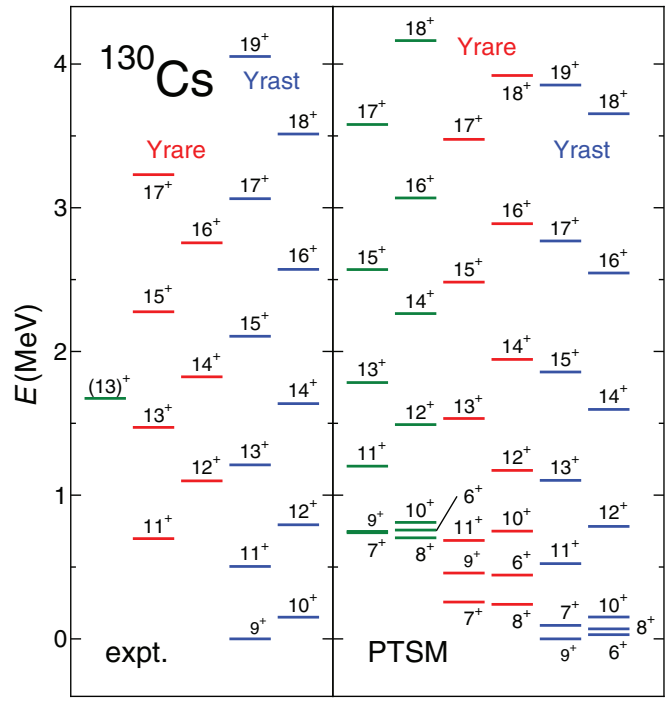

FIG. 3. (Color online) Same as Fig. 2, but for ^{130}Cs. The experimental data are taken from Refs. [5,7,47,48].

parameter $b = 1.005A^{1/6}$ fm in Eq. (12). The adopted values of the gyromagnetic ratios and the effective charges are the same as used in the previous PTSM calculations [29].

In Fig. 6, the theoretical transition ratios $B(M1; I \to I-1)/B(E2; I \to I-2)$ along the yrast states for all the doubly-odd nuclei are shown together with the experimental data. In the case of ^{132}Cs, the theoretical transition ratios of the 13_1^+, 15_1^+, and 17_1^+ states are larger compared to the experimental ones, but the staggering pattern is in phase. In the cases of ^{130}Cs and ^{134}La, the large-amplitude staggering of the $B(M1)/B(E2)$ ratios are in excellent agreement with the experimental data, except for the 16_1^+ state of ^{134}La. This anomalous behavior might be due to band crossing between the yrast band and the yrare band. As an indication, irregular level sequences in the yrast bands were reported on the neighboring Pr isotopes [51–53]. In particular, the positive-parity yrast bands with the $\nu h_{11/2} \otimes \pi h_{11/2}$ configuration in ^{134}Pr exhibit irregular level sequences due to band crossing at spins 15 and 16 [51]. In the case of ^{132}La, the PTSM calculation successfully reproduces the basic staggering feature, but the staggering amplitude of the theoretical $B(M1)/B(E2)$ ratios is larger compared with that of the experimental ones. This is a delicate problem and by changing the wave functions slightly we may reproduce the experimental data. There is a conjecture that the staggering phenomenon is closely related to the deformation of the core (even-even part of the nucleus) as discussed in Ref. [31]. There it is conjectured that the staggering becomes weak when the system approaches to the well-deformed nucleus. This issue is further examined in Sec. V.

In Fig. 7, the theoretical $B(E2; I \to I-2)$ values for the yrast and yrare states of all the doubly-odd nuclei are shown as functions of spin I. The strong $E2$ transitions connect the yrast

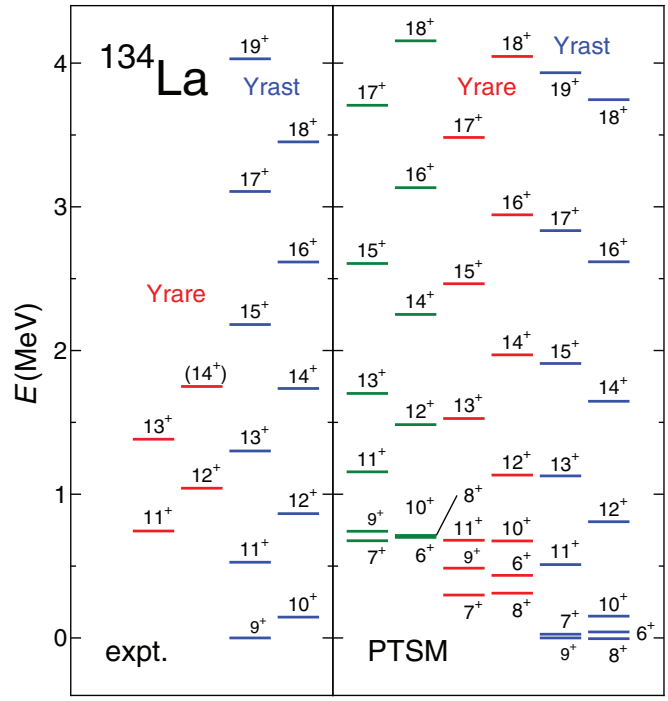

FIG. 4. (Color online) Same as Fig. 2, but for ^{134}La. The experimental data are taken from Refs. [3,49].

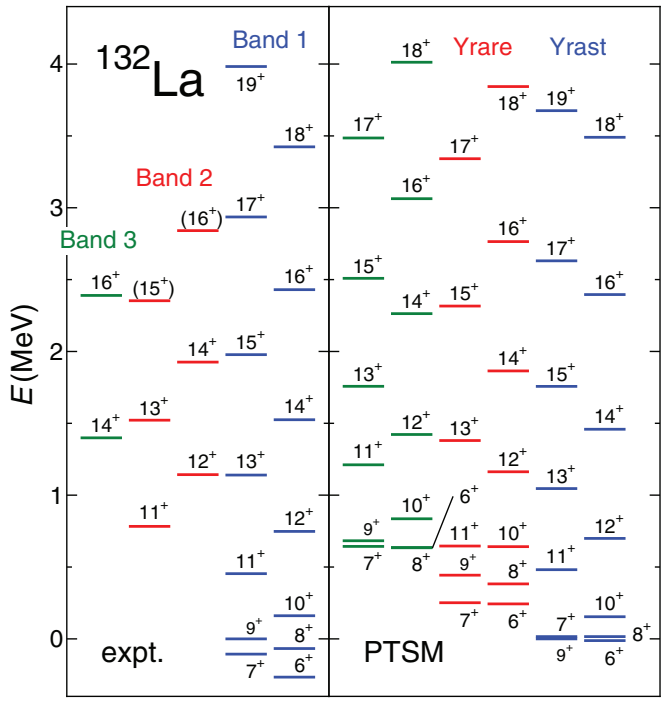

FIG. 5. (Color online) Same as Fig. 2, but for ^{132}La. The experimental data are taken from Refs. [4,9,44,50].

states with spin I ($I \geqslant 12$) to the yrast states with spin $I-2$. In contrast, the $B(E2)$ values are found to be small from the yrast states to the yrare states ($I \geqslant 12$). Thus, the strong $E2$ transitions for the yrast states indicate that the even-spin and the odd-spin states, respectively, form two $\Delta I = 2$ $E2$ bands starting from the bandhead states of 10_1^+ and 11_1^+. For the yrare states, the odd-spin states ($I \geqslant 11$) and the even-spin states ($I \geqslant 12$) are respectively linked by the strong $E2$ transitions.

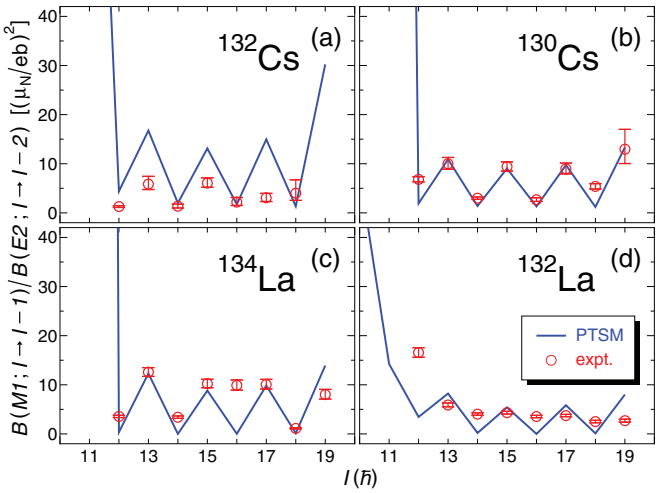

FIG. 6. (Color online) Comparison between experimental $B(M1)/B(E2)$ ratios of yrast states and those in PTSM for (a) ^{132}Cs, (b) ^{130}Cs, (c) ^{134}La, and (d) ^{132}La. The experimental data are taken from Refs. [3,4,6,7].

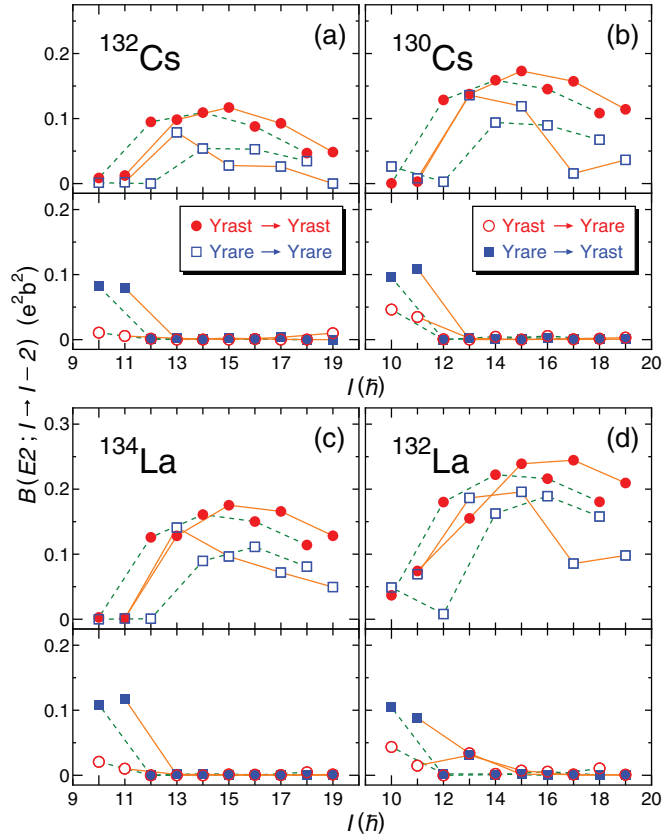

FIG. 7. (Color online) Theoretical $B(E2; I \to I-2)$ values for (a) ^{132}Cs, (b) ^{130}Cs, (c) ^{134}La and (d) ^{132}La. The filled circles, open squares, open circles and filled squares represent the transitions between yrast states, between yrare states, from yrast to yrare states and from yrare to yrast states, respectively. Solid lines indicate the transitions between the odd-spin states, and the dotted line indicates the transitions between even-spin states. In the lower panel for each nucleus, the yrast states with spin I and the yrare states with spin $I-2$ are connected by solid or dotted lines.

For the transitions from the yrare states to the yrast states, the $B(E2; 11_2^+ \to 9_1^+)$ and $B(E2; 10_2^+ \to 8_1^+)$ values are the largest compared with other transitions for all the nuclei. On the basis of the theoretical $B(E2)$ values, the odd-spin states ($9_1^+, 11_2^+, 13_2^+, 15_2^+$) and the even-spin yrare states respectively form two $\Delta I = 2$ $E2$ bands with their bandhead states of 9_1^+ and 12_2^+. From analysis of the $B(E2)$ values, we conclude that the following members form five $\Delta I = 2$ $E2$ bands, each starting from the first member as the bandhead state: (a) 11_1^+, $13_1^+, 15_1^+, 17_1^+$; (b) $10_1^+, 12_1^+, 14_1^+, 16_1^+$; (c) $9_1^+, 11_2^+, 13_2^+, 15_2^+$ (15_3^+ for ^{132}Cs); (d) $8_1^+, 10_2^+$; (e) $12_2^+, 14_2^+, 16_2^+$.

In Fig. 8, the calculated $B(M1; I \to I-1)$ values of the yrast states and the yrare states for ^{132}Cs, ^{130}Cs, ^{134}La and ^{132}La are shown as functions of spin I. For all the nuclei, the $B(M1)$ values between the yrast states ($I \geqslant 11$) are large for the transitions from the odd-spin states to the even-spin states, and small for the transitions from the even-spin states to the odd-spin states. In contrast, for both cases $B(M1)$ values are found to be small for the yrare states ($I \geqslant 12$). Furthermore, with respect to the other $\Delta I = 1$

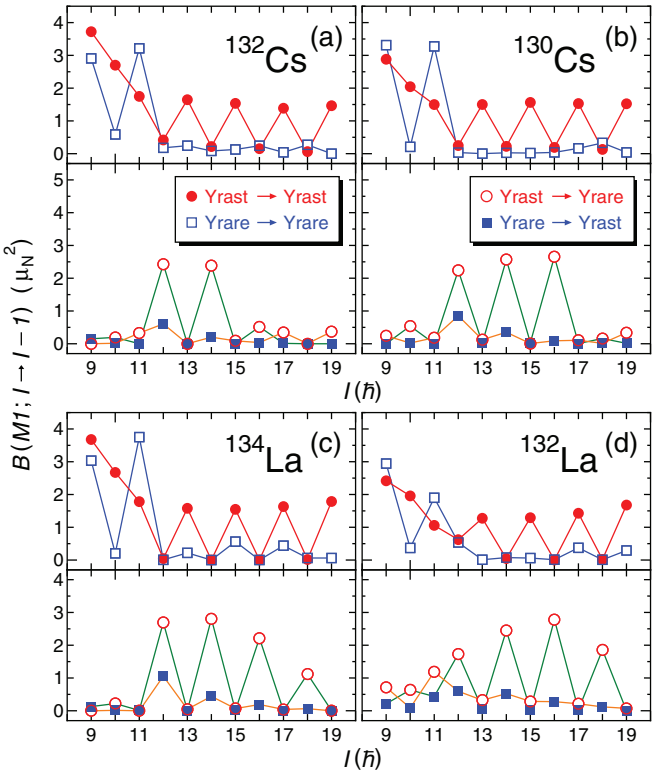

FIG. 8. (Color online) Theoretical $B(M1; I \rightarrow I-1)$ values for (a) ^{132}Cs, (b) ^{130}Cs, (c) ^{134}La, and (d) ^{132}La. The filled circles, open squares, open circles, and filled squares represent the transitions between yrast states, between yrare states, from yrast to yrare states, and from yrare to yrast states, respectively. In the lower panel for each nucleus, the yrast states with spin I and the yrare states with spin $I-1$ are connected by solid lines.

transitions, large $B(M1)$ values ($\gtrsim 0.40\mu_N^2$) are predicted for the $10_1^+ \rightarrow 9_1^+ \rightarrow 8_1^+$, $12_1^+ \rightarrow 11_2^+ \rightarrow 10_2^+$, $14_1^+ \rightarrow 13_2^+$, and $16_1^+ \rightarrow 15_2^+$ ($16_1^+ \rightarrow 15_3^+$ for ^{132}Cs) transitions in all the nuclei. [$B(M1; 16_1^+ \rightarrow 15_3^+) = 2.01\mu_N^2$ for ^{132}Cs.] These strong $M1$ transitions indicate that the $\Delta I = 1$ $M1$ bands are composed of the following four level sequences: (1) 8_1^+, 9_1^+, 10_1^+, 11_1^+; (2) 10_2^+, 11_2^+, 12_1^+, 13_1^+; (3) 13_2^+, 14_1^+, 15_1^+; (4) 15_2^+ (15_3^+ for ^{132}Cs), 16_1^+, 17_1^+.

The partial level scheme of ^{134}La constructed from the results of the $M1$ and $E2$ transition rates is shown in Fig. 9. We do not display other figures, but similar level schemes are deduced also for ^{132}Cs, ^{130}Cs, and ^{132}La. The PTSM gives five $\Delta I = 2$ $E2$ bands starting from the bandhead states of 8_1^+, 9_1^+, 10_1^+, 11_1^+, and 12_1^+. The states within bands are connected by the strong $M1$ transitions to the same members of the $\Delta I = 2$ $E2$ bands, and by the strong $M1$ transitions to the states in the neighboring $\Delta I = 2$ $E2$ bands. Here, it should be noted that the structure of the even-spin yrare states (12_2^+, 14_2^+, and 16_2^+) are quite different from those of the other $\Delta I = 2$ $E2$ bands, since these states are not connected by the strong $M1$ transitions to any member of other $\Delta I = 2$ $E2$ bands. The detailed analysis of their structure is presented in Sec. V.

C. Energy spectra of other low-lying states

In this paper our main concern is the structure of the yrast and yrare states built on the $\nu h_{11/2} \otimes \pi h_{11/2}$ configuration. However, one of the advantages of the PTSM is to simultaneously describe the low-lying positive-parity and negative-parity states other than those states on the unique-parity $0h_{11/2}$ valence neutron and/or proton orbitals. In Figs. 10–13, theoretical energy levels arising from the unpaired nucleons with positive-parity are compared with the experimental data for ^{132}Cs, ^{130}Cs, ^{134}La, and ^{132}La. For ^{134}La, the position of the 9_1^+ state with the $\nu h_{11/2} \otimes \pi h_{11/2}$ configuration relative to the ground state with positive parity (the 1_1^+ state) remains unknown.

In experiment, the ground states are assigned to have positive parity for ^{132}Cs, ^{130}Cs, and ^{134}La, while in ^{132}La the ground state is assigned to have negative parity, and the lowest state with positive parity, the $(2)^+$ state, has an excitation energy of 0.155 MeV. In the cases of ^{132}Cs, ^{134}La, and ^{132}La, the calculated levels agree with the experimental ones and, especially, the spins and parities of the ground states are reproduced. In the case of ^{130}Cs, the theoretical 1_1^+ state appears higher in energy than the experimental one. However, the theoretical levels of the 1_1^+, 2_1^+, 2_2^+, 2_1^-, and 5_1^- states are in reasonable correspondence with the experimental data.

D. Comparison between present results and our previous results

Now we compare the present numerical results with our previous calculations in the PTSM [27] and the quadrupole coupling model (QCM) [30,31]. The previous PTSM calculation reproduced successfully the relative energies between the ground states with positive parity and the states with the $\nu h_{11/2} \otimes \pi h_{11/2}$ configuration. However, the theoretical lowest states based on the $\nu h_{11/2} \otimes \pi h_{11/2}$ configuration were located at excitation energies of 1.75, 1.79, 1.29, and 1.34 MeV in ^{132}Cs, ^{130}Cs, ^{134}La, and ^{132}La, respectively, which are rather high in energy compared with the experimental data. In contrast, as shown in Figs. 10–13, the present PTSM calculations almost perfectly reproduce their relative positions. Moreover, a good correspondence with experiment is achieved for the energy levels of the negative-parity states. With respect to the electromagnetic transition rates, the previous PTSM results were already in good agreement with the experimental staggering feature of the $B(M1)/B(E2)$ ratios, although a slight difference between theory and experiment in absolute values was seen. However, in the present study, the PTSM gives a better description of the absolute values for the $B(M1)/B(E2)$ ratios (shown in Fig. 6), especially for ^{130}Cs and ^{132}La.

The PTSM is a quantum theoretical framework which incorporates both particle number and angular-momentum conservation. However, it has a practical limit due to particle number. At present we need to limit the particle number up to nine due to the computational capability. In contrast the quadrupole coupling model (QCM) provides a reasonable theoretical framework to describe the doubly-odd nuclei in place of the PTSM. In this model the core representing the even-even part of the nucleus couples with a neutron and a proton in

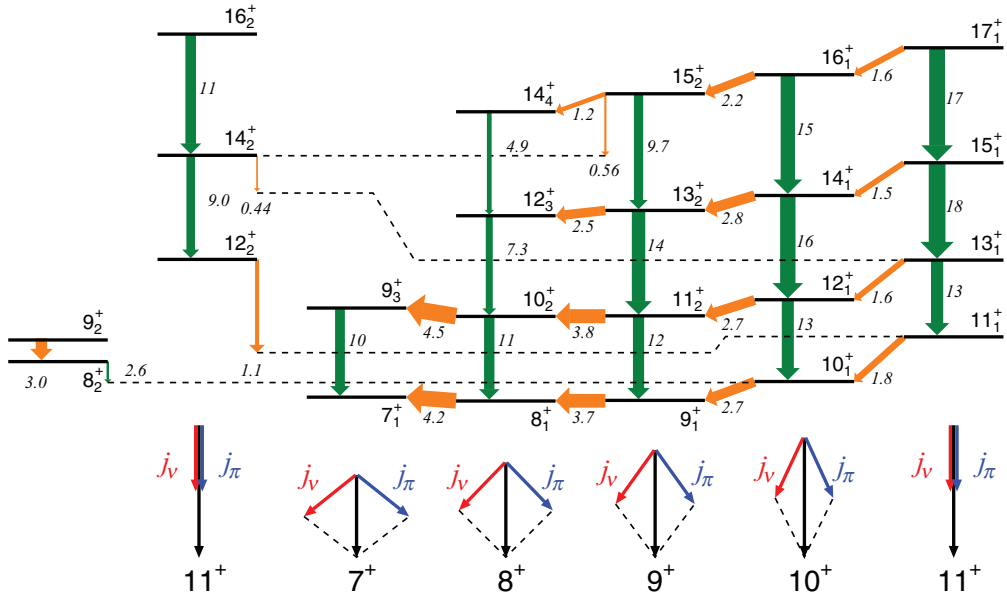

FIG. 9. (Color online) Partial level scheme of ^{134}La suggested by the PTSM calculation. The green arrows indicate $E2$ transitions [$B(E2) \geqslant 0.02e^2b^2$], and the orange arrows denote $M1$ transitions [$B(M1) \geqslant 0.40\mu_N^2$]. The numerals on the right side of the $E2$ transitions denote the $B(E2)$ values (in $10^{-2}e^2b^2$), and those beneath the $M1$ transitions denote the $B(M1)$ values (in μ_N^2). Schematic illustrations of the chopsticks configurations are presented below each $\Delta I = 2$ $E2$ band. The red and the blue arrows indicate the angular momenta of the neutron and the proton for the bandhead state, respectively. Six $\Delta I = 2$ $E2$ bands have the configurations shown by the schematic illustrations below.

the high-j intruder orbitals through a quadrupole-quadrupole interaction. The QCM calculations were performed for the doublet bands in the mass $A \sim 130$ region, and excellent agreement was obtained for both energy spectra and features of electromagnetic transitions [30,31]. Due to its simple applicability, the QCM can be applied to doublet bands for a wide range of doubly-odd nuclei, but instead deals only with the states built on the high-j orbitals of a neutron and a proton. Moreover, interaction strengths must be adjusted to reproduce the energy levels of the doublet bands. In contrast, the PTSM can systematically treat even-even, odd-mass, and doubly-odd nuclei on the equal footing. It should be noted that the energy

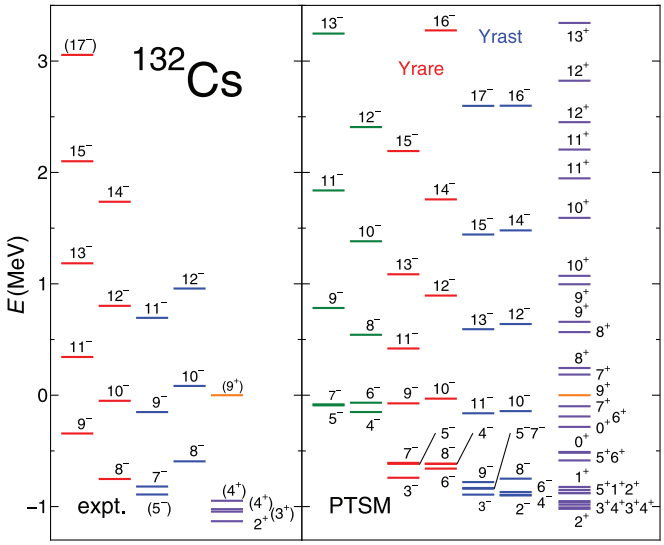

FIG. 10. (Color online) Comparison of experimental energy levels (expt.) with the PTSM results (PTSM) for ^{132}Cs. For the PTSM results, two level sequences of $\Delta I = 2$ on the left represent the negative-parity states arising from the unpaired positive-parity neutron, and four level sequences of $\Delta I = 2$ in the middle represent the negative-parity states arising from the unpaired positive-parity proton. The level sequences on the right denote the positive-parity states arising from the unpaired nucleons with positive-parity. The experimental data are taken from Refs. [44–46].

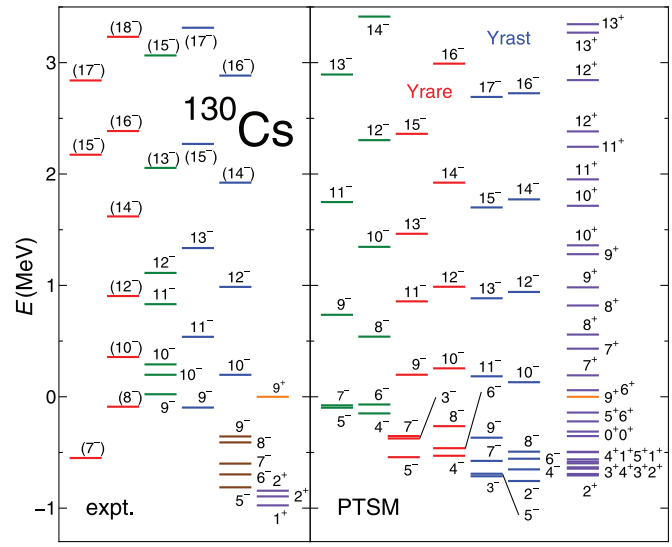

FIG. 11. (Color online) Same as Fig. 10, but for ^{130}Cs. The experimental data are taken from Refs. [5,7,47,48].

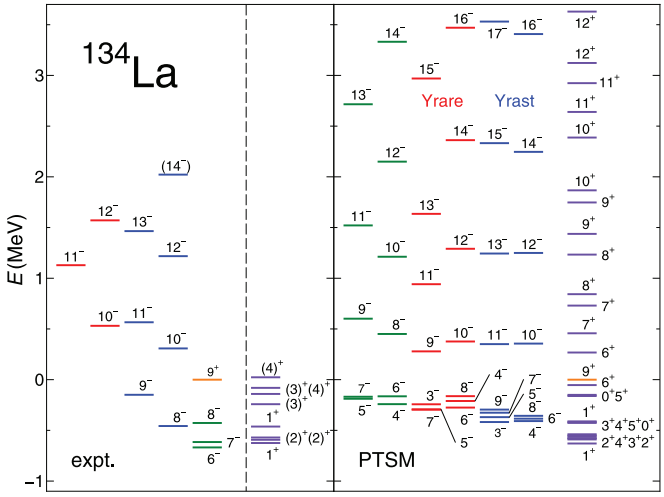

FIG. 12. (Color online) Same as Fig. 10, but for ^{134}La. The experimental data are taken from Refs. [3,49].

levels and the electromagnetic transition rates for the doublet bands are thus naturally obtained in the present PTSM study.

For the description of the doublet bands, the energy spectra obtained by the present PTSM calculations give almost the same results as those of the QCM results [30,31]. However, with respect to the low-lying states with spins less than 9, the PTSM gives better agreement with experiment than the QCM. Moreover, except for ^{132}La, the staggering amplitudes of the $B(M1)/B(E2)$ ratios in the present PTSM study are in better agreement with the experimental data. In spite of the above differences between the QCM and the PTSM, the picture for the doublet bands remains the same in both models.

V. ANALYSIS OF WAVE FUNCTIONS

A. Specific configurations

A detailed understanding of the structure of the yrast and yrare states with the $\nu h_{11/2} \otimes \pi h_{11/2}$ configuration can be achieved by examining the wave functions. For even-even nuclei, it is useful to calculate the expectation values of the numbers of various collective pairs. However, since the PTSM wave functions for doubly-odd nuclei are rather complicated and composed of various components in doubly-odd nuclei, we need another way of analyzing their wave functions. In the present study, we construct the wave functions of a *specific configuration* in the shell-model space and calculate the overlaps between them and the doubly-odd nuclear states given in Eq. (16). From the previous studies [26–28,30,31], it is understood that the main structure of the yrast and yrare states of the doubly-odd nuclei in the mass $A \sim 130$ region is described in terms of a weak coupling of the *chopsticks configurations* [26–28], which represent two angular momenta of the unpaired neutron and the unpaired proton, to the quadrupole collective excitations of the even-even part of the nucleus. Thus, we construct the *specific configuration* by adding one neutron hole and one proton particle both in the $0h_{11/2}$ orbital to an even-even nuclear state, which is obtained by the diagonalization of the shell-model Hamiltonian in the S and D pair subspace. The specific configuration with total spin I is defined as

$$|\Psi(LR_i;I)\rangle = \frac{1}{\sqrt{\langle LR_i;I|LR_i;I\rangle}}\,|LR_i;I\rangle\,, \qquad (24)$$

with

$$|LR_i;I\rangle = [|j_\nu j_\pi;L\rangle \otimes |R_i\rangle]^{(I)}\,, \qquad (25)$$

where L represents the angular momentum of the two-particle state of one neutron hole and one proton particle $|j_\nu j_\pi;L\rangle$, and $|R_i\rangle$ is the wave function for the ith state with spin R of the even-even nucleus (the even-even core). The energy spectra are shown in Fig. 1. A detailed description is given in the Appendix. The probabilities of finding the specific configuration $|\Psi(LR_i;I)\rangle$ in the doubly-odd nuclear state $|I^\pi\eta\rangle$ is

$$P\,(LR_i;I\eta) = |\langle I^\pi\eta|\Psi(LR_i;I)\rangle|^2\,. \qquad (26)$$

We denote the component of the state $|\Psi(LR_i;I)\rangle$ shortly as (L, R_i) in the following.

In Tables II–IV, the overlap probabilities between the components (L, R_i) and the yrast and yrare states built on the $\nu h_{11/2} \otimes \pi h_{11/2}$ configuration are shown for ^{134}La. We do not discuss other nuclei, since similar results are obtained also for ^{132}Cs, ^{130}Cs, and ^{132}La. For the yrast states up to spin 11, the 11^+_1, 10^+_1, 9^+_1, and 8^+_1 states are principally made of the components $(11, 0_1)$, $(10, 0_1)$, $(9, 0_1)$, and $(8, 0_1)$, respectively. Although the component $(10, 2_1)$ in the 11^+_1 state is not negligible, we can say that the 0^+_1 component (the ground state of ^{134}Ba) plays an important role in describing these states and that the two-particle state of one neutron hole and one proton particle carry a dominant part of the total spin of doubly-odd nucleus (^{134}La).

In the appendix of Ref. [27], effective angles were calculated between two angular momenta of the neutron hole and the proton particle in the $0h_{11/2}$ orbital. The effective angle θ for the two-particle state of the neutron and the proton with angular momenta $L = 11$, 10, 9, and 8 turns out to be 32°, 57°, 75°, and 90°, respectively. The effective angles never become

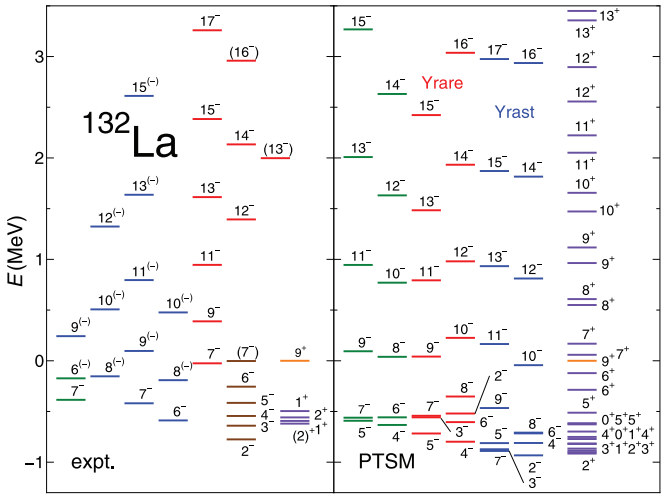

FIG. 13. (Color online) Same as Fig. 10, but for ^{132}La. The experimental data are taken from Refs. [4,9,44,50].

TABLE II. Overlap probabilities $P(LR_i; I\eta)$ (in percentage) of the components (L, R_i) for the yrast and yrare states with spins $I = 8$, 9, 10, and 11 in ^{134}La. Only the values with probability larger than 5% are shown. The main components are indicated in bold font.

I^π_η	$(8, 0_1)$	$(9, 0_1)$	$(10, 0_1)$	$(11, 0_1)$	$(7, 2_1)$	$(8, 2_1)$	$(9, 2_1)$	$(10, 2_1)$	$(11, 2_1)$	$(8, 4_1)$	$(9, 4_1)$	$(9, 2_2)$	$(10, 2_2)$
8^+_1	**43**				7		16						
8^+_2					**22**	14	11	11			5		
9^+_1		**42**				7	5	17					
9^+_2						**27**	11	16					
10^+_1			**44**				15		11				
10^+_2						**47**						13	
11^+_1				**41**				29					
11^+_2							**51**			5			12

zero because of quantum fluctuations, even though two angular momenta point in the same direction. From the above results on the effective angles, the 8^+_1 state of ^{134}La is constructed from perpendicular coupling of the two angular momenta of the neutron hole and the proton particle, while the 11^+_1 state is built by their parallel coupling.

Concerning the yrare states up to spin 11, the 11^+_2, 10^+_2, 9^+_2, and 8^+_2 states are made mainly of the components $(9, 2_1)$, $(8, 2_1)$, $(8, 2_1)$, and $(7, 2_1)$, respectively. In contrast to the yrast states, the 2^+_1 component (the 2^+_1 state of ^{134}Ba) is dominant among other components.

Next we focus our attention on the states which contain the same even-even core with higher angular momenta ($R = 2$, 4, and 6). The odd-spin yrast states (I) ($I = 13$, 15, and 17), the even-spin yrast states ($I - 1$), and the odd-spin yrare states ($I - 2$) are built mainly on the $L = 11$, 10, and 9 configurations, respectively. This means that the two angular momenta of the neutron and proton, like a pair of chopsticks, close with increasing total spin I for the states with the same even-even core. Furthermore, it is found that the simple sum of the angular momenta of the even-even core (R) and the two-particle state (L) is equal to the total spin ($I = R + L$). In other words, they have parallel configurations of the angular momenta of the even-even core and the two-particle state. For the other states, the 12^+_2, 14^+_2, and 16^+_2 states are mainly made of the $L = 11$ component. They are different from the 13^+_1, 15^+_1, and 17^+_1 states, since the angular momenta of the even-even core and the two-particle state point in different directions from each other.

As discussed in Sec. IV B, the large $B(E2)$ values obtained by the PTSM calculations form five $\Delta I = 2$ $E2$ bands each starting from the first member as the bandhead state: (a) 11^+_1, 13^+_1, 15^+_1, 17^+_1; (b) 10^+_1, 12^+_1, 14^+_1, 16^+_1; (c) 9^+_1, 11^+_2, 13^+_2, 15^+_2; (d) 8^+_1, 10^+_2; (e) 12^+_2, 14^+_2, 16^+_2. The members of each $\Delta I = 2$ $E2$ band are made mainly of the same chopsticks configurations. In Fig. 9, schematic illustrations of the chopsticks configurations are presented below each $\Delta I = 2$ $E2$ band. For instance, the 11^+_1, 13^+_1, 15^+_1, and 17^+_1 states [band (a)] have the parallel chopsticks configuration with angular momentum 11, while the 8^+_1 and 10^+_2 states have the perpendicular chopsticks configuration with angular momentum 8. The large $E2$ transition rates along the $\Delta I = 2$ $E2$ band are interpreted to come from the collective excitations of the even-even part of the nucleus. In particular, the yrast states (the 0^+_1, 2^+_1, 4^+_1, and 6^+_1 states) of the even-even core become dominant.

For the large $M1$ transition rates, the following members form four $\Delta I = 1$ $M1$ bands: (1) 8^+_1, 9^+_1, 10^+_1, 11^+_1; (2) 10^+_2, 11^+_2, 12^+_1, 13^+_1; (3) 13^+_2, 14^+_1, 15^+_1; (4) 15^+_2, 16^+_1, 17^+_1. These large $M1$ transition rates are explained in the following way: The members of each $\Delta I = 1$ $M1$ band are built mainly on the same even-even core. Then, the two angular momenta of the neutron and the proton close with increasing spin I within each $\Delta I = 1$ $M1$ band. For instance, the 10^+_2, 11^+_2, 12^+_1, 13^+_1 states [band (2)] have mainly the $R_i = 2_1$ component. The pair of chopsticks closes as spin I increases, causing strong $M1$ transition rates between them.

Now let us discuss the difference between the chiral scheme and that of the PTSM. In the chiral picture [10,11], the total angular momentum is tilted with respect to the planes defined by the three principal axes, i.e., the short, long, and intermediate axes of the triaxial core. This situation is realized when the

TABLE III. Same as Table II, but for the yrast and yrare states with spins $I = 12$, 13, and 14.

I^π_η	$(10, 2_1)$	$(11, 2_1)$	$(9, 4_1)$	$(10, 4_1)$	$(11, 4_1)$	$(9, 6_1)$	$(10, 6_1)$	$(10, 2_2)$	$(11, 2_2)$	$(9, 3_1)$	$(10, 3_1)$	$(11, 3_1)$	$(10, 4_2)$	$(10, 4_3)$
12^+_1	**58**		9						8					
12^+_2		**39**		5				24		5				
13^+_1		**67**		16										
13^+_2			**52**								12			5
14^+_1				**64**		5						5		
14^+_2					**50**		5						17	

TABLE IV. Same as Table II, but for the yrast and yrare states with spins $I = 15$, 16, and 17.

I^{π}_{η}	$(11,4_1)$	$(9,6_1)$	$(10,6_1)$	$(11,6_1)$	$(9,8_1)$	$(10,4_2)$	$(10,5_1)$	$(11,5_1)$	$(11,6_2)$	$(10,7_1)$	$(10,6_3)$	$(11,6_3)$	$(11,6_4)$	$(10,7_2)$
15^+_1	**78**		8											
15^+_2		**30**				21	23							
16^+_1			**65**					9						
16^+_2				**61**							7			
17^+_1				**80**					6					
17^+_2					7				19	12		13	**21**	12

angular momenta of the valence particle, the valence hole, and the triaxial core tend to align with the short, long, and intermediate axes, respectively. This implies that the unpaired neutron and the unpaired proton are strongly coupled to compose the characteristic configuration of their angular momenta, even for the high-spin yrast states. However, the physical situation realized in the PTSM largely deviates from the ideal chiral picture. In the PTSM calculations, the odd-spin yrast states with spins greater than 11 are made by totally parallel coupling of the two angular momenta of the neutron and proton. Since the sum of the angular momenta of the even-even core (R), and the two-particle state (L) is equal to the total spin ($I = R + L$), three angular momenta of the core, the neutron, and the proton point toward the same direction. It indicates that the doublet bands are so constructed that the chopsticks configurations are weakly coupled with the quadrupole collective excitations of the even-even part of the nucleus.

B. Staggering origin of $M1$ transitions

In order to understand the staggering origin of the $M1$ transition rates for yrast states, we take up simplified wave functions for the doubly-odd nuclear states. For example, we consider the weak $M1$ transition from the 12^+_1 state to the 11^+_1 state and the strong $M1$ transition from the 11^+_1 state to the 10^+_1 state. Through the analysis of the wave functions, we can assume that each state is made mainly of one component. They are expressed as

$$|12^+, 1\rangle = \alpha|(L, R+2)\rangle + \cdots, \tag{27}$$

$$|11^+, 1\rangle = \beta|(L+1, R)\rangle + \cdots, \tag{28}$$

$$|10^+, 1\rangle = \gamma|(L, R)\rangle + \cdots, \tag{29}$$

where α, β, and γ represent the amplitudes of the main components $(L, R+2)$, $(L+1, R)$, and (L, R) (here $L = 10$ and $R = 0$), respectively, and the contribution from the remaining parts $+\cdots$ are expected to be small. Then the reduced matrix elements for the $M1$ transition operator in Eq. (21) can be written as

$$\langle 11^+, 1\|\hat{T}(M1)\|12^+, 1\rangle \approx \alpha\beta\langle(L+1, R)\|\hat{T}(M1)\|(L, R+2)\rangle, \tag{30}$$

$$\langle 10^+, 1\|\hat{T}(M1)\|11^+, 1\rangle \approx \beta\gamma\langle(L, R)\|\hat{T}(M1)\|(L+1, R)\rangle. \tag{31}$$

Thus the reduced matrix element $\langle(L+1, R)\|\hat{T}(M1)\|(L, R+2)\rangle$ in Eq. (30) vanishes because the core angular momenta (R and $R+2$) differ by two units for the components $(L+1, R)$ and $(L, R+2)$; namely, the $M1$ operator $\hat{T}(M1)$ does not connect different angular-momentum states of the core. On the other hand, the reduced matrix element $\langle(L, R)\|\hat{T}(M1)\|(L+1, R)\rangle$ in Eq. (31) can remain finite because the core angular momenta are the same for both the components (L, R) and $(L+1, R)$, and the $M1$ operator $\hat{T}(M1)$ does connect the different angular-momentum two-particle states $|L\rangle$ and $|L+1\rangle$. These facts clearly show that the large interband $M1$ transition rates come only by closing the two angular momenta of the neutron and the proton as if a pair of chopsticks close.

This analysis also explains why, in general, the staggering amplitude of the $B(M1)/B(E2)$ ratios becomes weaker when the system approaches a well-deformed region. In well-deformed nuclei the components $(L, R+2)$, $(L+1, R)$, and (L, R) are almost equally mixed and it is expected that the $B(M1)$ selection rules discussed above do not apply.

C. Interpretation of level structure

Finally, we give a shell-model interpretation for the level structure of the doublet bands. The bandhead states of the $\Delta I = 2$ $E2$ bands are built on the chopsticks configurations of one neutron hole and one proton particle both in the $0h_{11/2}$ orbitals. From a property of the QQ interaction between neutrons and protons, the chopsticks configuration with angular momentum 8 becomes the lowest state, and the excitation energy of a chopsticks configuration increases as the angular momentum of the coupled neutron and proton becomes larger, as given in the appendix of Ref. [27]. The collective excitations of each $\Delta I = 2$ $E2$ band are built on the yrast states of the even-even core (weak coupling limit).

Here we consider the limiting case in which there is no interaction between the chopsticks configurations and the even-even cores. This situation leads to the spectrum shown in Fig. 14, each energy of which is obtained just by simply adding both the energy of a chopsticks configuration and the energy of a yrast state of the even-even core. The spins of these states are also obtained by the simple sum of the angular momenta of the chopsticks configurations and the even-even cores. This means that these angular momenta point in the same direction. This is an ideal situation. In reality the doublet bands are so constructed that the chopsticks configurations are weakly coupled with the quadrupole collective excitations of the even-even part of the nucleus, because the configuration

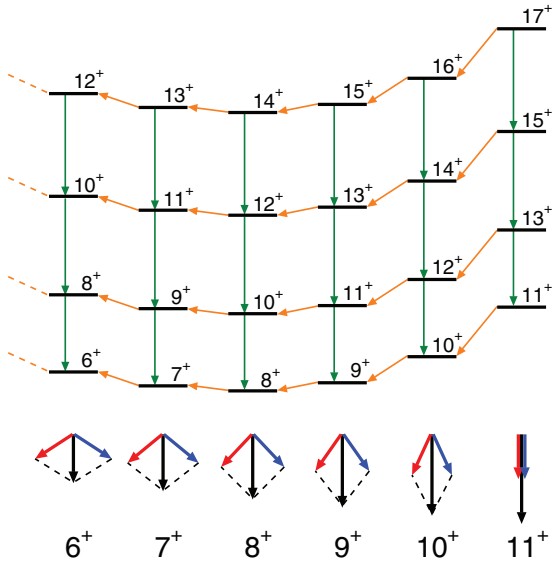

FIG. 14. (Color online) Band scheme predicted by the PTSM calculation in weak-coupling limit. The vertical arrows from top to bottom indicate $E2$ transitions, and the horizontal arrows from right to left indicate $M1$ transitions. Schematic illustrations of the chopsticks configurations are presented below the band scheme.

mixing washes away this ideal band structure, especially at high energy.

VI. SUMMARY

In this work, we apply the pair-truncated shell model (PTSM) to the structure study of the four doubly-odd nuclei, ^{132}Cs, ^{130}Cs, ^{134}La, and ^{132}La. The main aim of our study is to investigate the internal structure of the doublet bands built on the $\nu h_{11/2} \otimes \pi h_{11/2}$ configuration. It is worth emphasizing that in our calculations we have consistently employed the same Hamiltonian as used in the previous systematic studies of $A \sim 130$ nuclei [29], without any modification. The PTSM calculations reproduce well the energy levels of not only the yrast and yrare states based on the $\nu h_{11/2} \otimes \pi h_{11/2}$ configuration, but also other states with positive and negative parities. The theoretical electromagnetic transitions agree well with the even-odd staggering nature of the ratios $B(M1; I \to I-1)/B(E2; I \to I-2)$ along the yrast line.

In order to examine the underlying physics for the yrast and yrare states, we construct the wave functions with *specific configurations* in the shell-model space and calculate the overlap probabilities between them and the PTSM wave functions of the doubly-odd nuclei. The *specific configuration* is so constructed by coupling the two-particle state of one neutron hole and one proton particle both in the $0h_{11/2}$ orbital to the even-even nuclear states which are obtained after diagonalizing the shell-model Hamiltonian in the SD subspace. The results of the probabilities show that the angular momenta of the neutron and the proton, like a pair of chopsticks, close with increasing spin I within each $\Delta I = 1$ $M1$ band [26–28]. This chopsticks motion provides the large $M1$ transition rates. In contrast, the large $E2$ transition rates along the $\Delta I = 2$ $E2$ band come from the collective excitations of the even-even core. Especially, the yrast states of the even-even core play important roles in describing the $\Delta I = 2$ $E2$ bands.

In conclusion, the experimentally identified yrast and yrare states with the $\nu h_{11/2} \otimes \pi h_{11/2}$ configuration are interpreted as arising from the chopsticks configurations, which represent the two angular momenta of the unpaired neutron and the unpaired proton, weakly coupled with the quadrupole collective excitations of the even-even core. The chopsticks configurations and the even-even core produce characteristic $\Delta I = 1$ $M1$ and $\Delta I = 2$ $E2$ bands.

ACKNOWLEDGMENTS

The numerical calculations financially supported by Saitama University were carried out partly by the Hitachi SR16000 supercomputers at the Supercomputing Division, Information Technology Center, University of Tokyo. This work was supported by a Grant-in-Aid for Scientific Research (C) No. 24540251 and No. 25400267 from the Japan Society for the Promotion of Science (JSPS).

APPENDIX: SPECIFIC CONFIGURATION OF EVEN-EVEN CORE AND TWO-PARTICLE STATE

In this appendix, we briefly describe how to construct a specific configuration of the even-even core and two-particle state. The creation operator of the two-particle state of one neutron in the j_1 orbital and one proton in the j_2 orbital is defined as

$$[c^\dagger_{j_1\nu} c^\dagger_{j_2\pi}]^{(L)}_M = \sum_{m_1 m_2} (j_1 m_1 j_2 m_2 | L M) c^\dagger_{j_1 m_1 \nu} c^\dagger_{j_2 m_2 \pi}, \tag{A1}$$

where L is the angular momentum of the two-particle state, and M is its projection. A many-body wave function of the even-even nucleus is written as

$$|R_i\rangle = \sum_{\eta_\nu, \eta_\pi} C(i, \eta_\nu \eta_\pi) [|R_\nu \eta_\nu\rangle \otimes |R_\pi \eta_\pi\rangle]^{(R)}, \tag{A2}$$

where $|R_\tau \eta_\tau\rangle$ ($\tau = \nu$ or π) is the SD-pair states given by Eq. (4) and $C(i, \eta_\nu \eta_\pi)$ is obtained by diagonalizing the shell-model Hamiltonian in Eq. (7).

Using the above creation operator and the many-body wave function, the even-even core plus two-particle state is constructed as

$$
\begin{aligned}
|LR_i;I\rangle &= \left[\left[c^\dagger_{j_1\nu}c^\dagger_{j_2\pi}\right]^{(L)}|R_i\rangle\right]^{(I)} \\
&= \sum_{\eta_\nu,\eta_\pi} C(i,\eta_\nu\eta_\pi)\left[\left[c^\dagger_{j_1\nu}c^\dagger_{j_2\pi}\right]^{(L)}[|R_\nu\eta_\nu\rangle\otimes|R_\pi\eta_\pi\rangle]^{(R)}\right]^{(I)} \\
&= \sum_{\eta_\nu,\eta_\pi} C(i,\eta_\nu\eta_\pi)\sum_{J_\nu J_\pi}\sqrt{(2L+1)(2R+1)(2J_\nu+1)(2J_\pi+1)}\begin{Bmatrix} j_1 & j_2 & L \\ R_\nu & R_\pi & R \\ J_\nu & J_\pi & I \end{Bmatrix}\left[\left[c^\dagger_{j_1\nu}|R_\nu\eta_\nu\rangle\right]^{(J_\nu)}\otimes\left[c^\dagger_{j_2\pi}|R_\pi\eta_\pi\rangle\right]^{(J_\pi)}\right]^{(I)},
\end{aligned}
\tag{A3}
$$

with

$$
[c^\dagger_j|R\eta\rangle]^{(J)}_M = \sum_{m_1m_2}(jm_1Rm_2|JM)c^\dagger_{jm_1}|Rm_2\eta\rangle. \tag{A4}
$$

Since this state is usually not normalized, the specific configuration in Eq. (24) is normalized as

$$
|\Psi(LR_i;I)\rangle = \frac{1}{\sqrt{\langle LR_i;I|LR_i;I\rangle}}|LR_i;I\rangle. \tag{A5}
$$

[1] K. Starosta, T. Koike, C. J. Chiara, D. B. Fossan, D. R. LaFosse, A. A. Hecht, C. W. Beausang, M. A. Caprio, J. R. Cooper, R. Krücken, J. R. Novak, N. V. Zamfir, K. E. Zyromski, D. J. Hartley, D. L. Balabanski, J.-y. Zhang, S. Frauendorf, and V. I. Dimitrov, Phys. Rev. Lett. **86**, 971 (2001).

[2] A. A. Hecht, C. W. Beausang, K. E. Zyromski, D. L. Balabanski, C. J. Barton, M. A. Caprio, R. F. Casten, J. R. Cooper, D. J. Hartley, R. Krücken, D. Meyer, H. Newman, J. R. Novak, E. S. Paul, N. Pietralla, A. Wolf, N. V. Zamfir, J.-Y. Zhang, and F. Dönau, Phys. Rev. C **63**, 051302 (2001).

[3] R. A. Bark, A. M. Baxter, A. P. Byrne, G. D. Dracoulis, T. Kibédi, T. R. McGoram, and S. M. Mullins, Nucl. Phys. A **691**, 577 (2001).

[4] K. Starosta, C. J. Chiara, D. B. Fossan, T. Koike, T. T. S. Kuo, D. R. LaFosse, S. G. Rohoziński, C. Droste, T. Morek, and J. Srebrny, Phys. Rev. C **65**, 044328 (2002).

[5] T. Koike, K. Starosta, C. J. Chiara, D. B. Fossan, and D. R. LaFosse, Phys. Rev. C **67**, 044319 (2003).

[6] G. Rainovski, E. S. Paul, H. J. Chantler, P. J. Nolan, D. G. Jenkins, R. Wadsworth, P. Raddon, A. Simons, D. B. Fossan, T. Koike, K. Starosta, C. Vaman, E. Farnea, A. Gadea, T. Kröll, R. Isocrate, G. de Angelis, D. Curien, and V. I. Dimitrov, Phys. Rev. C **68**, 024318 (2003).

[7] A. J. Simons, P. Joshi, D. G. Jenkins, P. M. Raddon, R. Wadsworth, D. B. Fossan, T. Koike, C. Vaman, K. Starosta, E. S. Paul, H. J. Chantler, A. O. Evans, P. Bednarczyk, and D. Curien, J. Phys. G **31**, 541 (2005).

[8] S. Wang, Y. Liu, T. Komatsubara, Y. Ma, and Y. Zhang, Phys. Rev. C **74**, 017302 (2006).

[9] I. Kuti, J. Timár, D. Sohler, E. S. Paul, K. Starosta, A. Astier, D. Bazzacco, P. Bednarczyk, A. J. Boston, N. Buforn, H. J. Chantler, C. J. Chiara, R. M. Clark, M. Cromaz, M. Descovich, Z. Dombrádi, P. Fallon, D. B. Fossan, C. Fox, A. Gizon, J. Gizon, A. A. Hecht, N. Kintz, T. Koike, I. Y. Lee, S. Lunardi, A. O. Macchiavelli, P. J. Nolan, B. M. Nyakó, C. M. Petrache, J. A. Sampson, H. C. Scraggs, T. G. Tornyi, R. Wadsworth, A. Walker, and L. Zolnai, Phys. Rev. C **87**, 044323 (2013).

[10] S. Frauendorf and J. Meng, Nucl. Phys. A **617**, 131 (1997).

[11] V. I. Dimitrov, S. Frauendorf, and F. Dönau, Phys. Rev. Lett. **84**, 5732 (2000).

[12] T. Koike, K. Starosta, and I. Hamamoto, Phys. Rev. Lett. **93**, 172502 (2004).

[13] E. Grodner, J. Srebrny, A. A. Pasternak, I. Zalewska, T. Morek, C. Droste, J. Mierzejewski, M. Kowalczyk, J. Kownacki, M. Kisieliński, S. G. Rohoziński, T. Koike, K. Starosta, A. Kordyasz, P. J. Napiorkowski, M. Wolińska-Cichocka, E. Ruchowska, W. Płóciennik, and J. Perkowski, Phys. Rev. Lett. **97**, 172501 (2006).

[14] S. Brant, D. Vretenar, and A. Ventura, Phys. Rev. C **69**, 017304 (2004).

[15] E. Grodner, J. Srebrny, C. Droste, T. Morek, A. Pasternak, and J. Kownacki, Int. J. Mod. Phys. E **13**, 243 (2004).

[16] J. Srebrny, E. Grodner, T. Morek, I. Zalewska, J. Droste, Ch. Mierzejewski, A. A. Pasternak, J. Kownacki, and J. Perkowski, Acta Phys. Pol. B **36**, 1063 (2005).

[17] C. M. Petrache, G. B. Hagemann, I. Hamamoto, and K. Starosta, Phys. Rev. Lett. **96**, 112502 (2006).

[18] N. Yoshinaga, Nucl. Phys. A **503**, 65 (1989).

[19] N. Yoshinaga and D. M. Brink, Nucl. Phys. A **515**, 1 (1990).

[20] N. Yoshinaga, Nucl. Phys. A **570**, 421 (1994).

[21] N. Yoshinaga, T. Mizusaki, A. Arima, and Y. D. Devi, Prog. Theor. Phys. Suppl. **125**, 65 (1996).

[22] N. Yoshinaga, Y. D. Devi, and A. Arima, Phys. Rev. C **62**, 024309 (2000).

[23] K. Higashiyama, N. Yoshinaga, and K. Tanabe, Phys. Rev. C **67**, 044305 (2003).

[24] N. Yoshinaga and K. Higashiyama, Phys. Rev. C **69**, 054309 (2004).

[25] T. Takahashi, N. Yoshinaga, and K. Higashiyama, Phys. Rev. C **71**, 014305 (2005).

[26] K. Higashiyama and N. Yoshinaga, Prog. Theor. Phys. **113**, 1139 (2005).

[27] K. Higashiyama, N. Yoshinaga, and K. Tanabe, Phys. Rev. C **72**, 024315 (2005).

[28] N. Yoshinaga and K. Higashiyama, J. Phys. G **31**, S1455 (2005).
[29] K. Higashiyama and N. Yoshinaga, Phys. Rev. C **83**, 034321 (2011).
[30] N. Yoshinaga and K. Higashiyama, Eur. Phys. J. A **30**, 343 (2006); **31**, 395 (2007).
[31] K. Higashiyama and N. Yoshinaga, Eur. Phys. J. A **33**, 355 (2007).
[32] K. Higashiyama and N. Yoshinaga, Prog. Theor. Phys. **120**, 525 (2008).
[33] N. Yoshinaga and K. Higashiyama, J. Phys. G **37**, 115104 (2010).
[34] B. Fogelberg and J. Blomqvist, Nucl. Phys. A **429**, 205 (1984).
[35] M. Sanchez-Vega, B. Fogelberg, H. Mach, R. B. E. Taylor, A. Lindroth, J. Blomqvist, A. Covello, and A. Gargano, Phys. Rev. C **60**, 024303 (1999).
[36] W. J. Baldridge, Phys. Rev. C **18**, 530 (1978).
[37] W. Gelletly, W. R. Kane, and D. R. MacKenzie, Phys. Rev. C **9**, 2363 (1974).
[38] C. Girit, W. D. Hamilton, and E. Michelakakis, J. Phys. G **6**, 1025 (1980).
[39] T. Morek, H. Beuscher, B. Bochev, D. R. Haenni, R. M. Lieder, T. Kutsarova, M. Muller-Veggian, and A. Neskakis, Z. Phys. A **298**, 267 (1980).
[40] L. Goettig, C. Droste, A. Dygo, T. Morek, J. Srebrny, R. Broda, J. Styczeń, J. Hattula, H. Helppi, and M. Jiääskeläinen, Nucl. Phys. A **357**, 109 (1981).
[41] B. Fazekas, T. Belgya, G. Molnár, A. Veres, R. A. Gatenby, S. W. Yates, and T. Otsuka, Nucl. Phys. A **548**, 249 (1992).
[42] S. Juutinen, S. Törmänen, P. Ahonen, M. Carpenter, C. Fahlander, J. Gascon, R. Julin, A. Lampinen, T. Lönnroth, J. Nyberg, A. Pakkanen, M. Piiparinen, K. Schiffer, P. Šimeček, G. Sletten, and A. Virtanen, Phys. Rev. C **52**, 2946 (1995).
[43] A. Gade, I. Wiedenhöver, H. Meise, A. Gelberg, and P. von Brentano, Nucl. Phys. A **697**, 75 (2002).
[44] Y. Khazov, A. A. Rodionov, S. Sakharov, and B. Singh, Nucl. Data Sheets **104**, 497 (2005).
[45] T. Hayakawa, J. Lu, K. Furuno, K. Furutaka, T. Komatsubara, T. Shizuma, N. Hasimoto, T. Saitoh, M. Kidera, Y. Hatsukawa, and M. Oshima, Z. Phys. A **357**, 349 (1997).
[46] G. Rainovski, E. S. Paul, H. J. Chantler, P. J. Nolan, D. G. Jenkins, R. Wadsworth, P. Raddon, A. Simons, D. B. Fossan, T. Koike, K. Starosta, C. Vaman, E. Farnea, A. Gadea, T. Kröll, G. de Angelis, R. Isocrate, D. Curien, and V. I. Dimitrov, J. Phys. G **29**, 2763 (2003).
[47] B. Singh, Nucl. Data Sheets **93**, 33 (2001).
[48] R. Kumar, D. Mehta, N. Singh, H. Kaur, A. Görgen, S. Chmel, R. P. Singh, and S. Murlithar, Eur. Phys. J. A **11**, 5 (2001).
[49] A. A. Sonzogni, Nucl. Data Sheets **103**, 1 (2004).
[50] V. Kumar, P. Das, R. P. Singh, S. Muralithar, and R. K. Bhowmik, Eur. Phys. J. A **17**, 153 (2003).
[51] C. M. Petrache, D. Bazzacco, S. Lunardi, C. Rossi Alvarez, G. De Angelis, M. De Poli, D. Bucurescu, C. A. Ur, P. B. Semmes, and R. Wyss, Nucl. Phys. A **597**, 106 (1996).
[52] C. M. Petrache, C. A. Ur, D. Bazzacco, S. Lunardi, C. Rossi Alvarez, M. Ionescu-Bujor, A. Iordachescu, D. Bucurescu, F. Brandolini, G. de Angelis, G. Maron, D. R. Napoli, P. Pavan, N. H. Medina, R. Venturelli, S. Brant, and D. Vretenar, Nucl. Phys. **603**, 50 (1996).
[53] C. M. Petrache, S. Brant, D. Bazzacco, G. Falconi, E. Farnea, S. Lunardi, V. Paar, Z. Podolyák, R. Venturelli, and D. Vretenar, Nucl. Phys. A **635**, 361 (1998).